GEOPHYSICS, VOL. 87, NO. 4 (JULY-AUGUST 2022); P. B233–B245, 22 FIGS.
10.1190/GEO2021-0505.1

Case History

Building subsurface models with horizon-guided interpolation and deep learning: Application to the Volve field data

Shangsheng Yan[1], Xiaoming Sun[1], Xinming Wu[1], Sibo Zhang[2], and Hongjie Si[2]

ABSTRACT

Subsurface modeling plays an important role in hydrocarbon exploration but remains a challenging task that typically requires a full and reasonable integration of geophysical observations and geologic constraints. We have developed a workflow to fully use seismic amplitudes, well-log properties, and interpreted seismic structures to build geologically reasonable models. We take the Volve field data as an example and apply our workflow step by step as follows. First, we perform some preprocessing on the provided Volve seismic data, horizons, and well logs to remove anomalous values and adjust seismic-well ties in the depth domain. Second, we use a dynamic-programming-based method to infill gaps and refine the vertical positions of the provided horizons and efficiently pick more horizons. We further use the horizon surfaces to interpolate a relative geologic time (RGT) volume which can be considered as an implicit structural model representing seismic structural and stratigraphic features. Third, we integrate the provided well logs and the computed RGT volume to interpolate a subsurface model that conforms to well-log properties and seismic structural and stratigraphic features. Finally, we propose a multiscale neural network to predict a final subsurface model by using a combination of the seismic data and the interpolated model as inputs and using the well-log data as training labels. Inputting the interpolated model to the network helps to provide a low-frequency control for obtaining a more stable prediction. The results indicate that our workflow is able to produce geologically reasonable subsurface models with high lateral continuity and vertical resolution.

INTRODUCTION

Seismic data can provide stratigraphic features and geologic structure information, whereas well logs can provide high-resolution rock properties information in depth that is absent in seismic images. Therefore, jointly using well-log and seismic data is a feasible way to build subsurface models for reservoir characterization (e.g., Lemon and Jones, 2003; Zhu et al., 2012; Wu, 2017a).

Traditional methods use seismic structures and logging measurements to build models. Some of them take several horizons and major faults as constraints to construct a subsurface model (e.g., Mallet, 2002; Caumon et al., 2009). Others use image-guided interpolation to obtain models in accordance with seismic structures and well-logging data (e.g., Hampson et al., 2000; Hansen et al., 2008; Hale, 2010; Naeini and Hale, 2015; Karimi et al., 2017). These types of methods are improved by adding horizons or unconformities as additional constraints to interpolate a more accurate model (Naeini and Hale, 2015). In addition, some volumetric methods are proposed to integrate a full set of seismic horizons, faults, and unconformities to obtain a reasonable model (e.g., Jayr et al., 2008; Dorn, 2013; Souche et al., 2013, 2014; Mallet, 2014; Labrunye and Carn, 2015; Wu, 2017a). In all of these methods, seismic structural and stratigraphic features are used as guidance in well-log interpolation to build a rock property model that laterally honors seismic structures and properly approximates the low-frequency trend of subsurface properties but may fail to estimate laterally varying properties.

Manuscript received by the Editor 10 August 2021; revised manuscript received 12 February 2022; published ahead of production 19 March 2022; published online 16 May 2022.
[1]University of Science and Technology of China, School of Earth and Space Sciences, Hefei, China. E-mail: ssyan33@mail.ustc.edu.cn; urp@ustc.edu.cn; xinmwu@ustc.edu.cn (corresponding author).
[2]Huawei Cloud EI Product Department, Xi'an, China. E-mail: zhangsibo1@huawei.com; sihongjie@huawei.com.

DOI:10.1190/geo2021-0505.1

Such an interpolated model often is used as an initial or reference model in inversion schemes to obtain a more accurate rock property model by further fitting poststack or prestack seismic amplitudes. The inversion schemes can be typically classified into three types: sparse-spike-based methods (e.g., Oldenburg et al., 1983; Velis, 2008; Zhang and Castagna, 2011; Gholami and Sacchi, 2012; Yuan et al., 2015; Wang et al., 2016; Sui and Ma, 2019), model-based methods (e.g., Smith and Gidlow, 1987; Fu, 2004; Veeken and Da Silva, 2004; Wu, 2017b), and geostatistical or stochastic methods (e.g., Sen and Stoffa, 1991; Mallick, 1995; Ma, 2002; Buland and Omre, 2003; González et al., 2008; Bosch et al., 2010). These inversion methods often first make an assumption of some forward physical modeling to simulate synthetic seismic data from a desired rock property model and then invert for the model by optimally fitting the simulated data and recorded field data. However, the assumed forward modeling is often only an approximation and may not be able to fully simulate the recorded data, which typically limits the accuracy of the rock property estimation.

In recent years, deep learning (LeCun et al., 2015) has been successfully applied in inversion problems (e.g., Lucas et al., 2018; Tarhan and Akar, 2018; Sanghvi et al., 2020) and widely used in geophysics, such as seismic texture identification (e.g., Dramsch and Lüthje, 2018; Di et al., 2019), fault interpretation (e.g., Wu et al., 2019a, 2019b), and seismic horizon interpretation (e.g., Geng et al., 2020; Shi et al., 2020). For example, a supervised learning method called support vector regression is used to predict porosity and permeability (Al-Anazi and Gates, 2012). Convolutional neural networks (CNNs) are used to build subsurface velocity models (e.g., Araya-Polo et al., 2018; Wu and McMechan, 2018) and to predict seismic lithology (Zhang et al., 2018) or seismic impedance (e.g., Alfarraj and AlRegib, 2019; Biswas et al., 2019; Das et al., 2019; Mustafa et al., 2019; Puzyrev et al., 2019; Wang et al., 2019; Zheng et al., 2019). In addition, generative adversarial networks (Mosser et al., 2020) and recurrent neural networks (e.g., Alfarraj and AlRegib, 2018; Richardson, 2018) also are used for seismic inversion and petrophysical property estimation.

In this study, we have developed a workflow (Figure 1) to build a subsurface model by reasonably integrating interpreted seismic structures, seismic amplitudes, and well-log properties. We demonstrate the feasibility of our workflow on the public Volve data (Equinor, 2018). In our workflow, we first apply some corrections to the provided seismic data, horizons, and well logs to remove anomalous values. We then automatically improve the provided horizons by filling gaps and adjust them to more accurately follow seismic reflections. In addition to the provided horizons, we automatically pick more horizon surfaces throughout the entire seismic volume. We then calculate a relative geologic time (RGT) volume from the seismic horizons to implicitly represent seismic structural and stratigraphic features. We further interpolate an initial subsurface model from well logs by using an RGT-guided interpolation method. Such a model consistently follows seismic stratigraphic features and conforms to well-log properties. We propose a multiscale CNN with seismic traces and the initial model as inputs and logs as output. Finally, we predict a more accurate model by using seismic and well-log data, where the initial model also is input to the network to provide a low-frequency constraint for predicting stable results.

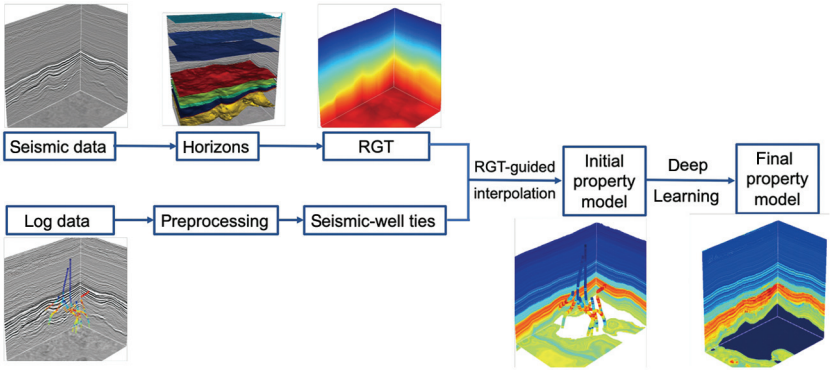

Figure 1. Our workflow applied to the Volve data set. We first apply some preprocessing to the provided seismic data, logs, and horizons. We then automatically extract more horizons to calculate an RGT volume that is used as structural guidance in well-log interpolation to obtain an initial reservoir property model. We finally apply a deep learning method to estimate a more accurate property model by using the initial model and seismic volume as inputs.

BACKGROUND OF VOLVE FIELD

Volve is a decommissioned field in the central part of the North Sea (Figure 2a) that was discovered in 1993. The plan for development and operation was approved in 2005. The field was shut down in 2016 and Equinor released the Volve Data Village data set for the purposes of research and study in June 2018 (Equinor, 2018). Its current license was based on the Creative Commons Attribution 4.0 International license but with some additions e.g., to disallow resale of the data set.

As shown in Figure 2a, the Volve field was located 5 km north of the Sleipner field with water depths of 80 m in the block 15/9. It was produced with water injection as pressure support and the produced oil was from sandstone in the Hugin Formation of the Jurassic age. The reservoir was located at 2750–3120 m true vertical depth subsea (TVDSS).

The geometry of this field is shown in Figure 2b. The field contains 5 TB of data over almost 40,000 files covering data such as production data, well design, completion string design, seismic data, well logs (petrophysical and drilling), geologic and stratigraphical data, static and dynamic models, and surface and grid data. The data set's 16.3 GB of well-log data, plots, and analyses covers 24 wellbores. Figure 3 shows a top view of all well logs.

In this paper, we mainly use the seismic (Figure 4a), horizons (Figure 4b), and well-log (Figure 3) data sets to build subsurface models. The seismic data are poststack migration in the depth domain, and therefore, we implement seismic calculation in the depth domain. The sample interval is 4 m. The first sample is 4 m, and the last sample is 4500 m. The seismic data are preprocessed with a series of steps developed by Kirch in 2011 called "ST10010ZC11_PZ_PSDM_KIRCH_FULL_D.-MIG_FIN.POST_STACK.3D.JS-017536.segy." The horizon data contain some key horizons such as Ty_Fm, Shetland_Gp, BCU, Hugin_Top, and Hugin_Base. The well-log data contain well perforation intervals and most important well picks for Volve wells.

SEISMIC HORIZONS

The first step of our workflow is to interpret seismic horizons from the seismic volume to construct the framework of the seismic structures. Such a structural framework is crucial for building subsurface models.

Horizon refinement

The 3D seismic image of the Volve field in the depth domain is shown in Figure 4a. Five horizons provided along with the seismic image are shown in Figure 4b. These horizons are laterally incomplete and are not accurate enough to follow consistent seismic phases. Therefore, we use a dynamic programming-based method (Yan and Wu, 2021) to fill the holes and refine the vertical positions of the provided horizons (Figure 4d). We also extract more horizons to compute a more accurate RGT volume in the next step. Figure 4c displays a cropped seismic image in which the shallow part and bad traces are removed.

To more clearly show the improvements of our horizon refinement, we display a single horizon before and after applying our refinement method in Figure 5. The target horizon of troughs is denoted by the green arrow in Figure 5a. The provided horizon is displayed in color in Figure 5b in which we observe that the horizon jumps between peaks and troughs. (The red color indicates troughs and the blue color indicates peaks.) Then, we use the dynamic programming method (Yan and Wu, 2021) to update the inaccurate horizon to the target horizon of seismic troughs by picking a nearby surface that passes through minimal amplitudes. As shown in Figure 5c, the updated horizon surface is red almost everywhere, which indicates that it follows consistent troughs. To further illustrate the changes between two horizons, we extract a 2D slice in the crossline-depth plane as shown in Figure 5d. The improved horizon (the green curve) obviously more accurately follows the target reflection than the provided one (the red curve).

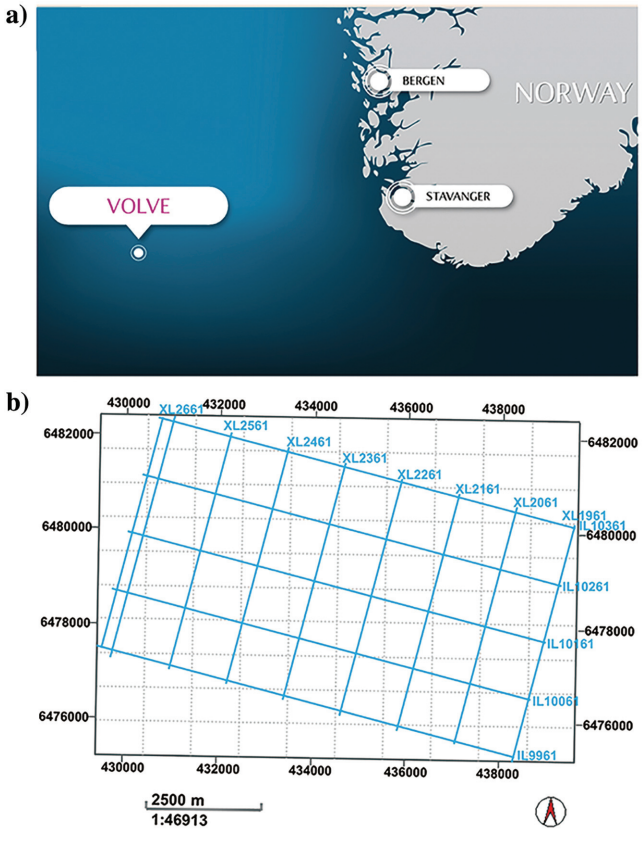

Figure 2. (a) The Volve field located at approximately 200 km west of Stavanger at the southern end of the Norwegian sector (modified from Equinor, 2018). (b) The geometry of seismic exploration.

Calculate RGT with horizons

The concept and generation of an RGT volume is explained by Stark (2003, 2005b). An RGT volume indicates geologic times at the locations corresponding to the seismic data samples. The RGT can be calculated with different methods, such as the phase-unwrapping method (e.g., Stark, 2003, 2006; Wu and Zhong, 2012), but a simple way is to interpolate an RGT volume from several horizons and seismic data (Stark, 2005a). Therefore, we first define an RGT for each of the picked horizons (Figure 4d). Then, the geologic time values between horizons are calculated by an interpolation algorithm, so that an RGT volume is obtained corresponding to the seismic volume (Figure 6). Such an interpolated RGT volume (Figure 6) can be considered as a 3D scalar field that implicitly represents structural features in the seismic volume (Figure 4c). The contours or isosurfaces of the RGT volume represent seismic horizons that generally follow seismic reflections. As this RGT volume is interpolated from a limited number of interpreted horizons (Figure 4d), it may not strictly honor all the detailed structures in the seismic image. However, this RGT volume is good enough to be used in the next step, which is to guide well-log interpolation to build a subsurface model that generally follows the seismic structures.

WELL LOGS

Well-log data are the basic data for establishing the initial model and the basis for geologic interpretation. It is the most accurate record characterizing the rock properties. There are 20 wells in the Volve Data Village with different properties such as velocity, density, impedance, gamma, and porosity (as listed in Figure 7). The impedance logs are calculated from the velocity and density logs. However, the well-log data quality is always affected by the borehole environment, such as wall collapse and mud immersion. In

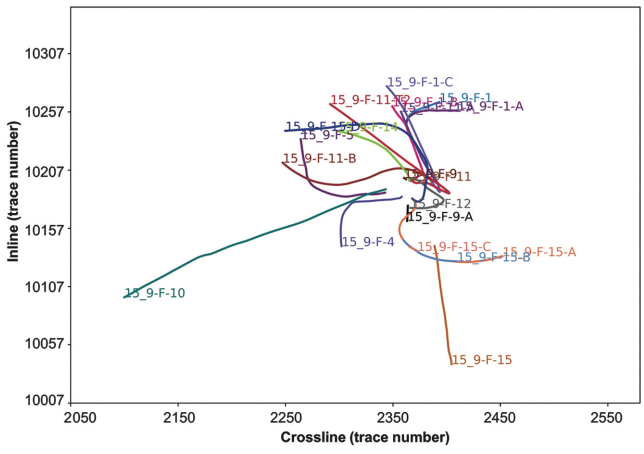

Figure 3. The top view of well logs in the Volve data.

addition, different measuring times and logging instruments also will affect well-log data to some degree. Therefore, we should first correct the potential errors or anomalies in the well-log data before using them to build subsurface models.

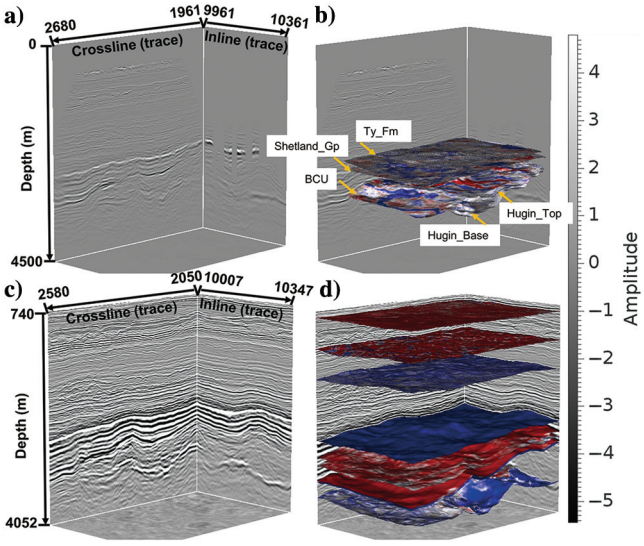

Figure 4. (a) The 3D seismic image in the Volve field. (b) The horizons provided along with the seismic image, which are laterally incomplete and are not accurate enough to consistently follow seismic reflections. (c) A cropped seismic image where the shallow part and bad traces are removed. (d) The provided horizons are improved (to more consistently follow seismic reflections and fill in the missing areas) and additional horizons are extracted by automatic methods.

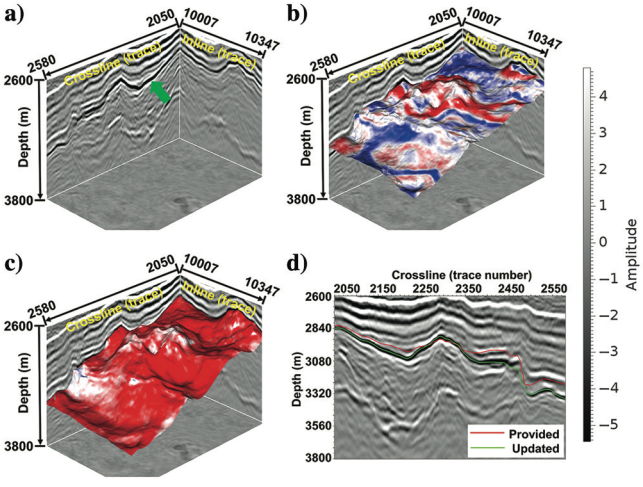

Figure 5. We choose a single horizon to more clearly show the effect before and after improvements. (a) A subvolume of the seismic image that contains the target horizon denoted by the green arrow. (b) One horizon provided along with the seismic image, which is not accurate enough to consistently follow seismic phases because the horizon jumps between peaks and troughs. (The red color indicates troughs and the blue color indicates peaks.) (c) The horizon is improved by our dynamic programming method, which more consistently follows troughs. (d) We extract a 2D slice in the crossline-depth plane. The improved horizon (the green curve) is more accurate than the provided horizon (the red curve).

Figure 8 shows an example of well-log curves. We mainly correct the distortion at the top and bottom of measurement section and anomalies at the connection of two logging curves as shown in Figure 8 (denoted by the red rectangle). In addition, some outliers (denoted by the black circles in Figure 8) must be removed because they will produce unreasonable anomalies in the postprocessing of seismic-well ties and training a neural network for rock property prediction.

Well-seismic ties also are important for joint seismic and well-log interpretation, which makes the rock properties measured at well locations consistent with seismic data. Although the seismic data are in the depth domain, we still need to make synthetic seismograms and perform horizon calibration to match the depths between well data and seismic data. Figure 9 displays an example of matching the synthetic and real seismograms for well-seismic ties. We choose the velocity $v(z)$ (the red curve) and density $\rho(z)$ (the green curve) logs in the same depth ranges as shown in Figure 9a. Then, the reflectivity series (Figure 9b) can be computed as follows (Sheriff and Geldart, 1995):

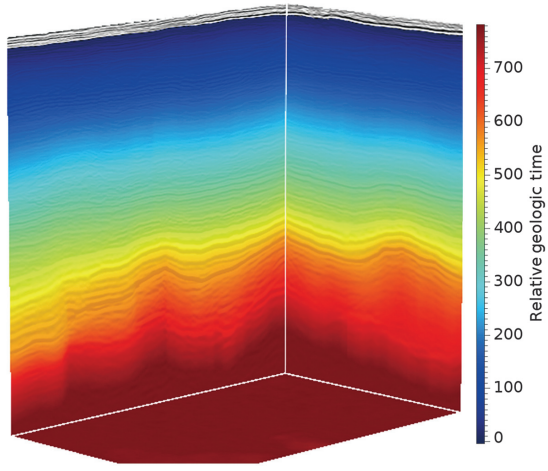

Figure 6. An RGT volume computed from seismic volume (Figure 4a) and interpreted horizons (Figure 4d).

Names / Properties	15_9-F-1	15_9-F-1-A	15_9-F-1-B	15_9-F-1-C	15_9-F-4	15_9-F-5	15_9-F-9	15_9-F-9-A	15_9-F-10	15_9-F-11-A
Velocity	√	√	√		√	√			√	√
Density	√	√	√	√	√	√			√	√
Impedance	√	√	√		√	√			√	√
Gamma	√	√	√	√	√	√	√	√	√	√
Porosity	√				√	√				

Names / Properties	15_9-F-11-B	15_9-F-11-T2	15_9-F-11	15_9-F-12	15_9-F-14	15_9-F-15	15_9-F-15-A	15_9-F-15-B	15_9-F-15-C	15_9-F-15-D
Velocity		√		√	√	√	√			
Density	√	√		√	√	√	√	√	√	
Impedance		√		√		√	√			
Gamma	√	√	√	√	√	√	√	√	√	√
Porosity				√	√	√	√	√		

Figure 7. There are 20 logs in the Volve Data Village with different properties, such as velocity, density, impedance, gamma, and porosity. Only six logs contain all five properties.

DOI:10.1190/geo2021-0505.1

$$r(z_i) = \frac{\rho(z_{i+1})v(z_{i+1}) - \rho(z_i)v(z_i)}{\rho(z_{i+1})v(z_{i+1}) + \rho(z_i)v(z_i)}, \quad (1)$$

where z_i indicates a depth sample.

Then, we choose a Ricker wavelet in the depth domain with the peak frequency of the real seismic data. The synthetic seismograms (Figure 9c) are obtained by convolving the reflectivity series with the wavelet. Finally, we adjust the seismic-well ties based on the alignment of the synthetic (the red waveforms) and real (the black waveforms) seismograms. After the seismic-well ties, the main reflectors are well matched as denoted by the yellow arrows in Figure 9d.

In Figure 10, we demonstrate the importance of the alignment between seismic and well-log data. We use the simple nearest interpolation following constant RGT values to obtain a velocity model (Figure 10b) according to the original 12 well logs as shown in Figure 10a. We can obviously observe some unreasonable discontinuities highlighted by the white arrows in Figure 10b because the well logs are inconsistent with the seismic data, which therefore leads to unreasonable interpolation results. After those preprocessing and well-seismic ties, the interpolated model shown in Figure 10c is more consistent with seismic reflectors except some areas denoted by the black circles. Figure 11 shows a 3D view of the seismic image with different types of well logs, where the same preprocessing has been applied to each type of log.

BUILDING MODELS

With the well-log properties after preprocessing, we first interpolate rock property models by using the previously computed RGT volume as structural guidance. We further design a CNN-based method to predict a more accurate property model with a combined input of the interpolated property model and the seismic amplitude volume. The interpolated model is used to provide the low-frequency components of the rock properties that are missing in the seismic amplitude data.

Initial models with RGT-guided interpolation

We integrate the provided well logs and the computed RGT volume to compute a subsurface model that conforms to well-log properties and seismic structural and stratigraphic features. We first interpolate the RGT values at the well-log points. Then, we interpolate the property values in the whole space $q(x, y, z)$ according to the RGT values $\tau(x, y, z)$ and the distance-based weights φ as follows:

$$q(x, y, z; \tau(x, y, z)) = \frac{1}{\sum_{i=1}^{k} \varphi_i} \sum_{i=1}^{k} w(x_i, y_i, z_i(\tau))\varphi_i, \quad (2)$$

where $w(x_i, y_i, z_i(\tau))$ represents a property sample measured in the ith well, and this log sample shares the same geologic time τ as the position to be interpolated. The interpolation weight φ_i is computed with a radial basis function of the lateral distance between the well position and the position to be interpolated:

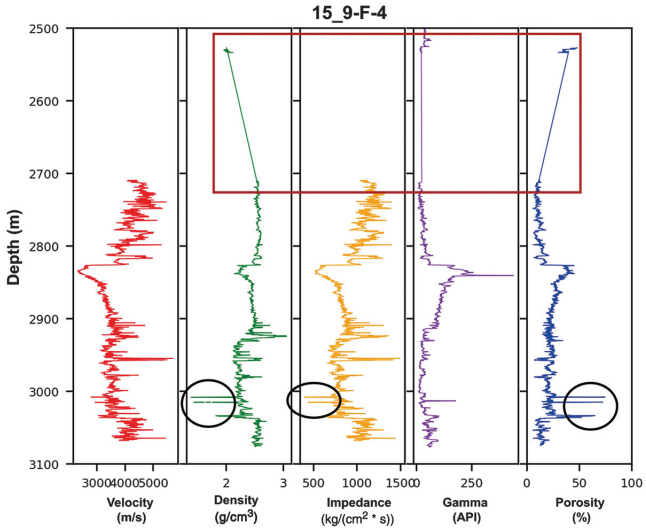

Figure 8. The recorded well-log data contain some outliers, missing parts (denoted by the red rectangle), or noisy spikes (denoted by the black circles). In addition, the sampling interval of well-log data is much smaller than that of seismic data and the well logs may not vertically align with the seismic data. Therefore, some preprocessing to the well-log data is necessary before subsurface modeling with seismic and well-log data.

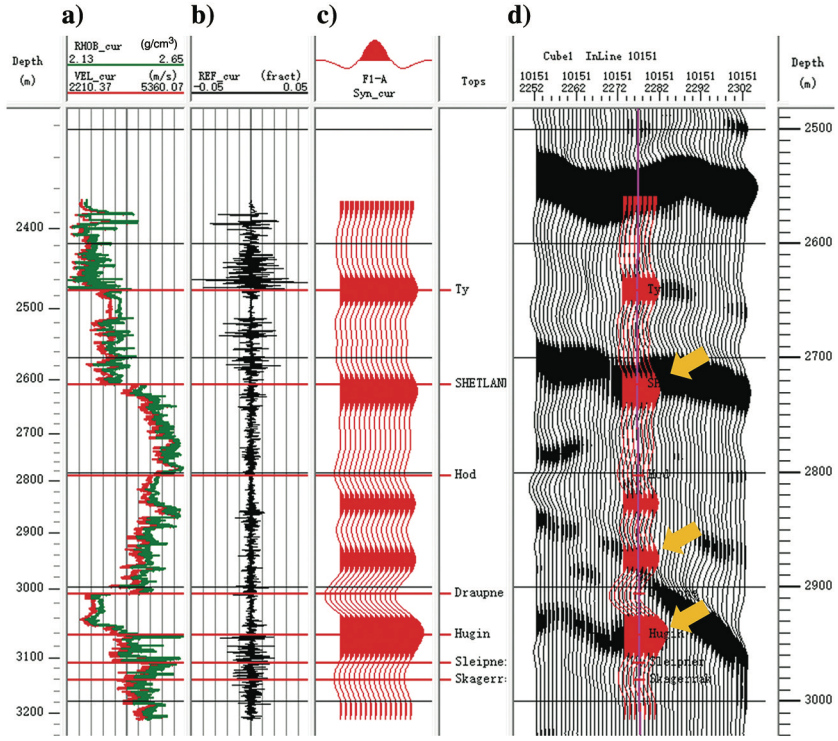

Figure 9. (a) From the velocity (the red curve) and density (the green curve) logs, we first calculate (b) a reflectivity sequence and then compute (c) a synthetic seismogram by convolving the reflectivity sequence with a Ricker wavelet. We finally adjust the seismic-well ties based on the alignment of the synthetic (the red waveforms) and real (the black waveforms) seismograms as shown in (d).

$$\varphi(i) = \frac{1}{1 + \varepsilon\sqrt{(x_i - x)^2 + (y_i - y)^2}}, \quad (3)$$

where ε is a shape parameter. In this RGT-based interpolation method, we implicitly implement a seismic structure-guided well-log interpolation by computing a weighted average of log samples belonging to the same geologic times or seismic stratal slices (horizons). Therefore, the interpolated model honors seismic structures that are implicitly represented in the RGT volume.

The first column of Figure 12 shows the initial models computed from different well-log properties using the RGT-guided interpolation. These initial models follow the seismic structures but are smooth and lack detail because the number of well logs is very limited. In addition, we may introduce incorrect information, especially in areas far from well locations because the rock property may significantly vary laterally and the RGT volume may not accurately follow structures. Therefore, we use the deep learning method in the next step to further improve the initial model to obtain a more accurate model with more details.

More accurate models with deep learning

In solving a geophysical inversion problem, an initial model often is provided and updated through iterations to obtain a reliable result. Inspired by this observation, we introduce the initial model (the first column of Figure 12) to our deep learning neural network to provide a low-frequency control in estimating a rock property model.

Data sets

This seismic amplitude volume (Figure 4c) is with the size of 828 (depth) × 530 (cross-line) × 340 (inline) samples. As shown in Figure 11, we prepare 12 velocity logs, 14 density logs, 12 impedance logs, 21 gamma logs, and nine porosity logs and choose one-third of each type of these logs as the validation set. Although the number of available logs is limited and they are measured at different depth ranges, we can still generate a large training data set by randomly extracting log segments with a fixed length. These log segments serve as 1D labels in training our neural network. The corresponding seismic traces and initial impedance sequences, extracted at the same locations and depth ranges, are concatenated together as a two-channel input to the neural network. Figure 13 shows an example of a training pair. The solid black curve (Figure 13a) represents a seismic trace. Figure 13b shows the real log (denoted by the red curve) and initial rock property (such as impedance that is denoted by the dashed black curve). The initial rock property curve serves as an input to the network, which can provide a low-frequency constraint to help predict more reliable results.

Network architecture

We consider the rock property estimation as a regression problem and propose a 1D network architecture (Figure 14) to solve such a regression problem. The input includes two channels with one seismic trace (the solid black curve) and one initial rock property (e.g., impedance) curve (the dashed black curve), and the output is the expected property curve (the red curve) as shown in Figure 14. The proposed network contains several multiscale

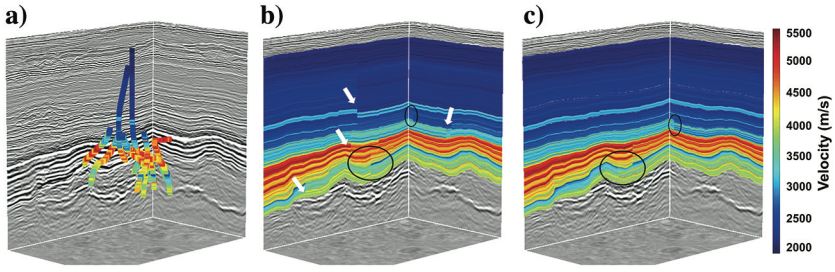

Figure 10. (a) Velocity logs are displayed with the 3D seismic image. (b) The RGT-guided nearest neighbor interpolation of these velocity logs is laterally discontinuous (highlighted by white arrows) along reflectors because the logs are not properly tied to the seismic image. (c) After applying some preprocessing to the well logs and adjustments to well-seismic ties, the model with nearest neighbor interpolation is more consistent with seismic reflectors except in the areas denoted by the black circles.

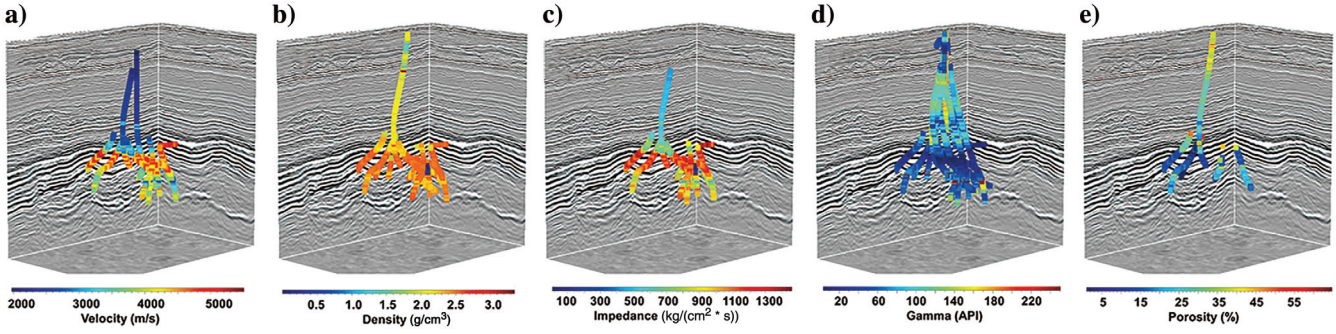

Figure 11. Different logs are shown in 3D seismic image: (a) 12 velocity logs, (b) 14 density logs, (c) 12 impedance logs, (d) 21 gamma logs, and (e) nine porosity logs.

DOI:10.1190/geo2021-0505.1

blocks with different kernel sizes to extract features from different scales. In our workflow, we use four multiscale blocks (Figure 14) with kernel sizes of 9, 13, and 23 samples, respectively, and each has 32 channels. Then, these output channels are concatenated to be used as an input to the next convolutional layer. We apply rectified liner unit (ReLU) activation function to the output of all convolution layers except the last one, on which we use a linear activation function.

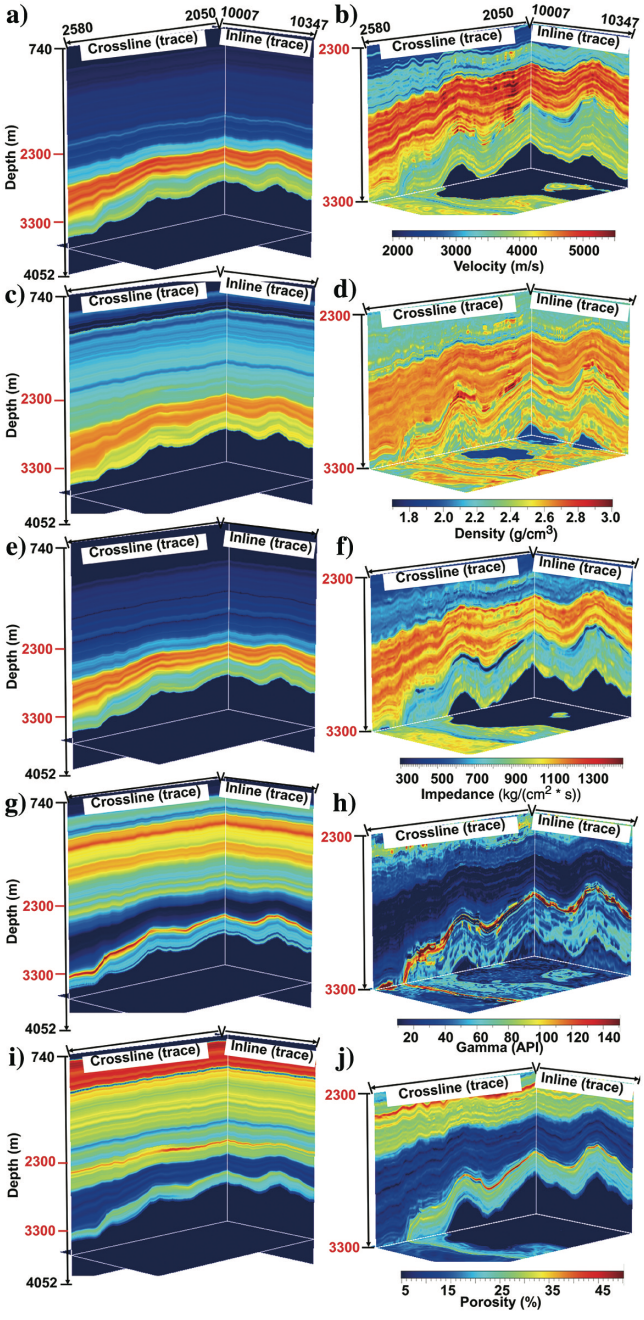

Figure 12. The initial and updated subsurface models with different properties. The first column shows initial models obtained by RGT-guided interpolation. The second column shows the final models predicted by our deep learning method. Note that in the second column we display only the target section in the depth range of 2300–3300 m to highlight the details.

For our regression problem, we use mean square error (MSE) loss to measure the errors between the ground truth and prediction:

$$L_2 = \frac{1}{N}\sum_{i=1}^{N}(p_i - r_i)^2, \tag{4}$$

where p_i and r_i represent the predicted and true impedance, respectively, and N represents the number of samples of one log. In our workflow, we use MSE loss function to evaluate the performance of the network.

Experiments

We apply our workflow to estimate subsurface models of different types of rock properties. Figure 15 shows the prediction and ground truth on validation sets of gamma logs. We observe that the predicted gamma values (the black curves) follow the general trend of the log (the red curves) under the interpolated constraint (the blue curves), and the prediction curves show more high-frequency features. For example, the predictions match the logs well at a depth of approximately 3000 m.

In Figure 12, we show the models predicted trace-by-trace by using the 1D CNN as shown in the second column. We mainly display the inverted results by deep learning at 2500–3200 m because the reservoir in the Volve field consists of Jurassic sandstones at 2750–3120 m TVDSS. The predictions obviously show high resolution in the depth direction for all property logs.

To view local details of the predicted results, we show a 2D seismic slice in crossline-depth section (the first row), the initial models (the second row), and the predicted results (the third row) in Figure 16. First, we observe that the predictions show more high-frequency features in the depth direction compared to the interpolation. This also certifies that the multiscale block with different kernel sizes can extract much richer features (denoted by the white arrows in Figure 16f and 16j). In addition, the predictions are consistent with seismic structure, which are more reasonable in the lateral directions. For example, we can see there is a fault in the seismic profile (denoted by the dashed black line in Figure 16); the distribution of sandstone layers and mudstone layers in the inversion profile is controlled by that fault. As a result, our inversion method is

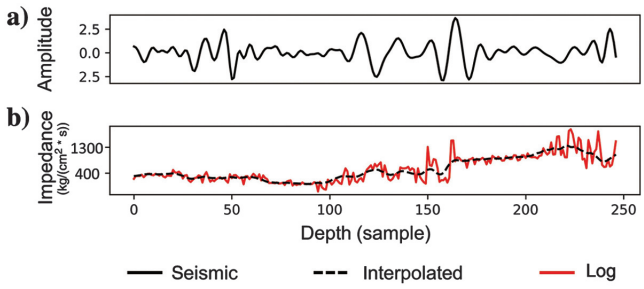

Figure 13. An example of a training pair. (a) The seismic trace. (b) The measured well-log property curve (the red curve) and the initial (interpolated) property curve (the dashed black curve). The seismic trace and initial rock property curve together serves as an input to our network, whereas the well-log property curve is the target of the network.

DOI:10.1190/geo2021-0505.1

consistent with the sequence stratigraphic framework and structure (Figure 16f, 16h, and 16j).

Figure 15 shows a comparison of the predicted rock property sequences at the four validation wells. Compared with the initially interpolated properties (the blue curves in Figure 15), our CNN-based predictions (black curves) show more details and visually match well with the ground truth (measured properties, denoted by the red curves in Figure 15). This observation is supported by the crossplots (Figure 17) between the measured well-log properties versus the predicted ones at the validation wells. From the crossplots, we observe that our predictions of all four types of rock properties (velocity, impedance, porosity, and gamma) show high correlations with the measured properties.

To further demonstrate the importance of the initial model as a low-frequency control, we show the test results based on the same network as shown in Figure 14 with only seismic data as inputs. In Figure 18, the 3D subsurface models obtained from only the seismic volume are shown in the first row and the second row shows 2D slices corresponding to Figure 16. The results show obvious horizontal discontinuities, lower resolution, and many vertical artifacts when compared with the results (Figures 12 and 16) with seismic data and the initial model as inputs.

In Figure 19, we also compare inversion results between the sparse-spike method and our deep learning method. Figure 19a shows a 2D seismic slice extracted from the 3D seismic volume. Figure 19b and 19c shows the inverted result by sparse-spike-based method and deep learning, respectively. Furthermore, Figure 19d shows the comparison of two logs obtained by our deep learning (the red curves) and the sparse-spike method (the blue curves). These results indicate that our method is more accurate and better fits well-log measurements (the black curves in Figure 19d).

GEOLOGIC INTERPRETATION

In this Volve survey, the structure and reservoirs deposition (Equinor, 2018) have been largely controlled by salt tectonics. Basically, salt was deposited during the late Permian, and the moving of salt, resulting from the Smith Bank and Skagerrak Formation (Triassic Formation) deposition, lead to differences in subsidence. Jurassic sedimentation started with the Sleipner Formation, then in the Middle Jurassic salt movement continued, and thick sand (Hugin Formation) filled in subsiding areas. The Heather Formation deposited after the sedimentation of the Hugin Formation. With the significant increase of organic productivity, the Draupne Formation, which is the source rock, sedimented after the Heather Formation.

In this working area, we mainly focus on the Hugin Formation sand (reservoirs) and the Draupne Formation (the source rocks) (Figure 20, modified from Equinor, 2018). The Hugin Formation in the Volve data set is mainly composed of marine sandstone, minor claystone, and limestone (e.g., Varadi et al., 1998; Kieft et al., 2010). Reservoirs in the Hugin Formation develop from 2750 to 3120 m (in TVDSS), and its thickness ranges from 20

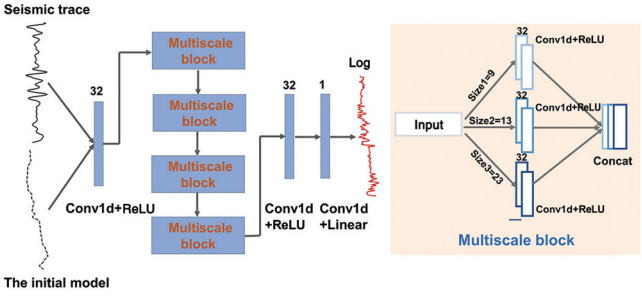

Figure 14. The CNN architecture with multiscale blocks. A multiscale block with different kernel size is designed to extract features from multiple scales. These features are then concatenated together and fed to the next convolutional layer.

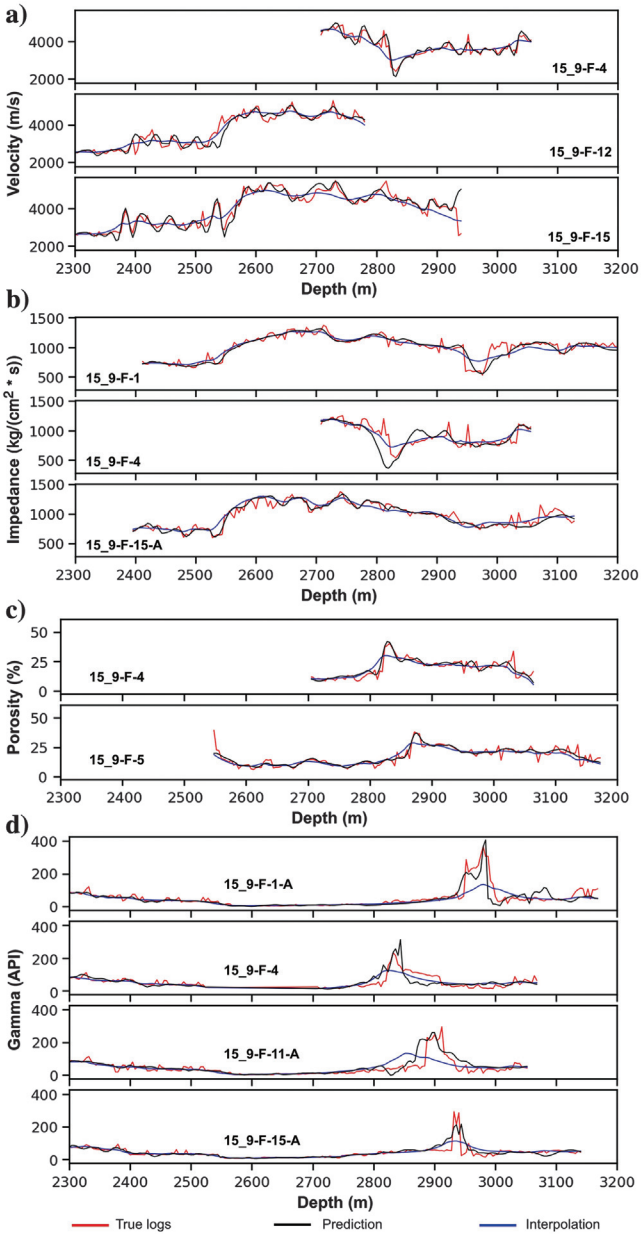

Figure 15. Reservoir property curves of (a) velocity, (b) impedance, (c) porosity, and (d) gamma predicted at the validation logs. The predictions (black curves) generally match well with the ground truth (well-log measurements denoted by the red curves).

DOI:10.1190/geo2021-0505.1

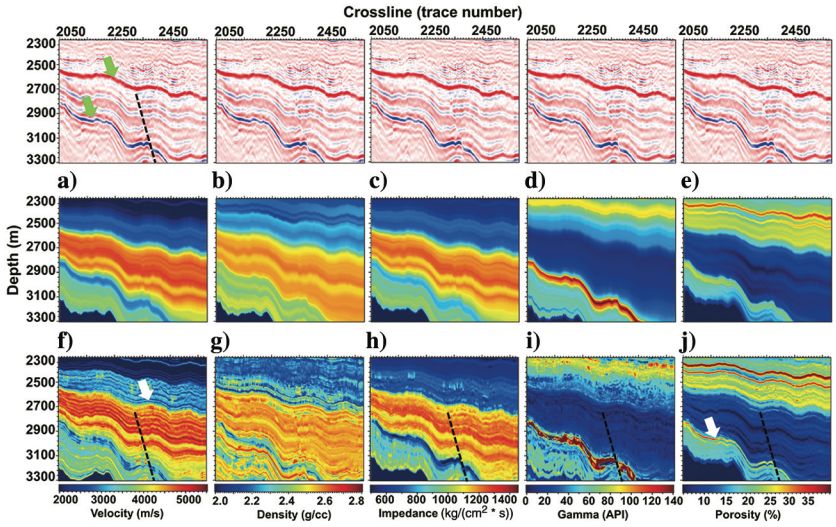

Figure 16. To view local details of predicted results, we show a 2D seismic slice (the first row), the initial models interpolated from well logs and an RGT volume (the second row), and the final results predicted by our CNN method (the third row). The predictions are consistent with seismic structures and show more high-frequency features (compared with the initial models) in the depth direction.

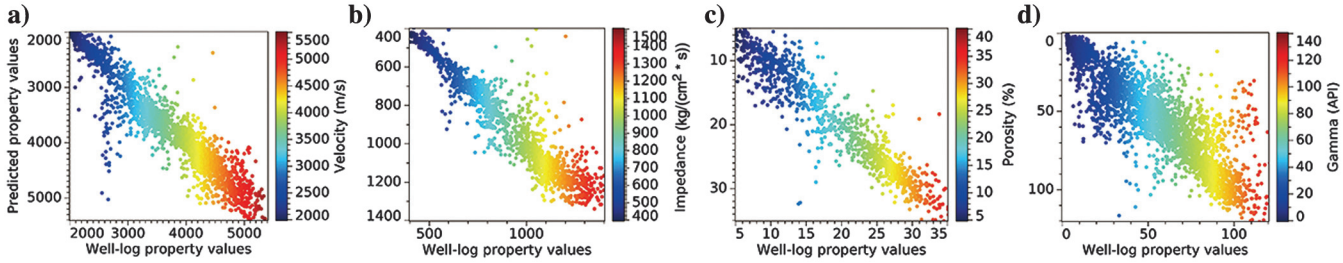

Figure 17. Crossplots at all log positions of different properties: the predicted property against the ground truth property. The results of velocity, impedance, and porosity show higher correlation than that of density and gamma.

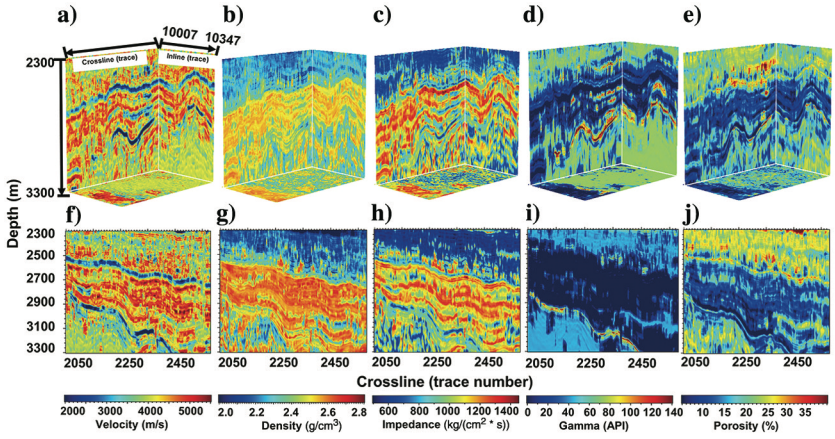

Figure 18. The results obtained from deep learning with only seismic data as inputs. The first row shows 3D subsurface models corresponding to the second column in Figure 12. The second row shows 2D slices corresponding to Figure 16. The results show horizontal discontinuities, lower resolution, and many vertical artifacts.

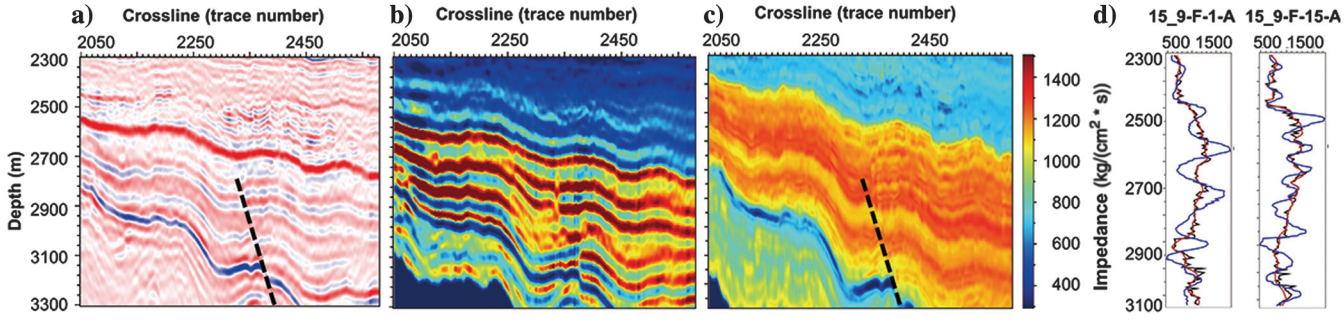

Figure 19. (a) A 2D seismic image extracted from the 3D seismic volume shown in Figure 4c. A comparison of (b) the traditional method based on sparse-spike and (c) deep learning. (d) Compared with the traditional method (the blue curves), our deep learning-based result (the red curves) better fits well-log measurements (the black curves) (with more reasonable low-frequency trend) and vertically shows more details.

to 100 m (Sen and Ganguli, 2019). Compared to the surrounding formations, reservoirs in the Hugin Formation are characterized by relatively high velocity, density, and impedance but low gamma and porosity. Petrophysics analysis shows that the gamma ray (GR) value of fine- to coarse-grained sandstone is from 10 to 46 API, sonic slowness (DT) value ranges from 175 to 315 μs/m, and bulk density (RHOB) ranges from 2.280 to 2.820 g/cm^3 (Kieft et al., 2010).

The thickness of reservoirs is affected by the movements of salt. In general, thickness is relatively small on salt highs and large in these subsiding zones. The well-logging data show that the Draupne claystone is characterized by extremely high gamma values and low impedance. In contrast, the Hugin sandstone reservoirs present low gamma value and relatively high impedance (Figure 20). The average porosity, permeability, and net to gross of the reservoirs are 0.21, 400 md, and 0.9, respectively.

The BCU (top of the Draupne Formation) and the top and bottom of the Hugin Formation are shown in Figure 21. The modeling result of Draupne source rocks shows that the claystone has relatively low impedance (Figure 21b) and high porosity (Figure 21c). High porosity (approximately 40%) might result from high formation pressure. For example, the pressure coefficient of source rocks at well 15_9-F-5 (near the top of BCU) could reach to 1.3 which is much higher than the pressure coefficient in the Hugin Formation (1.0) or the Hod Formation (1.02) (Equinor, 2018). In addition, we clearly see the difference between the very organic-rich claystone (Draupne Formation) and the claystone in the Heather Formation (beneath Draupne Formation). The Heather Formation claystone is characterized by a relatively lower porosity and higher impedance. Modeling results of the Hugin Formation present that the thick sand layers are widely deposited, and they are controlled by the structure highs (Figure 21b and 21c). According to the well-drilling data, well 15_9-F-5 encountered reservoirs with 144 m thickness from true vertical depth of 3055 to 3199 m. The sandstone has multiple claystone interbeds. From Figure 21b and 21c, we can see the variation of impedance and porosity which indicates the presence of these interbeds.

Figure 22 shows the stratal slicing of the top of the BCU and Hugin Formation. We see the overpressure areas of the source rocks (the high porosity areas in Figure 22a and 22b), which suggests that these source rocks are still generating hydrocarbons. The depositional environment of the Hungin Formation is tidal to shallow marine estuary. From the modeling results, we see potential tidal channels in the Hugin Formation (Figure 22c). In addition, the sandstone (the bottom left in Figure 22c–22e) might be tidal flat or tidal bar.

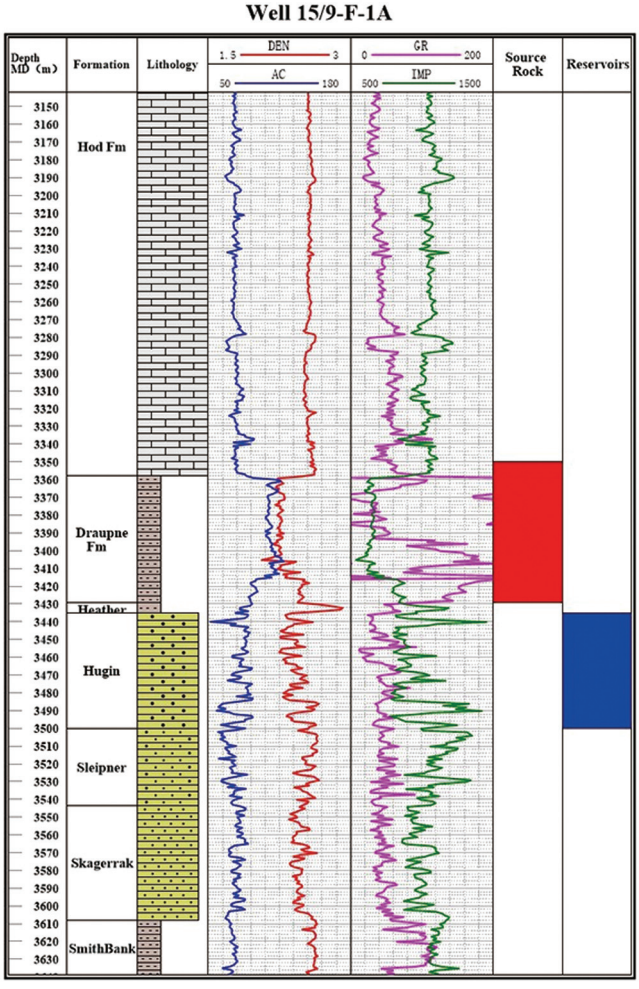

Figure 20. Well-log curves and lithology of well 15_9-F-1-A (from Equinor, 2018).

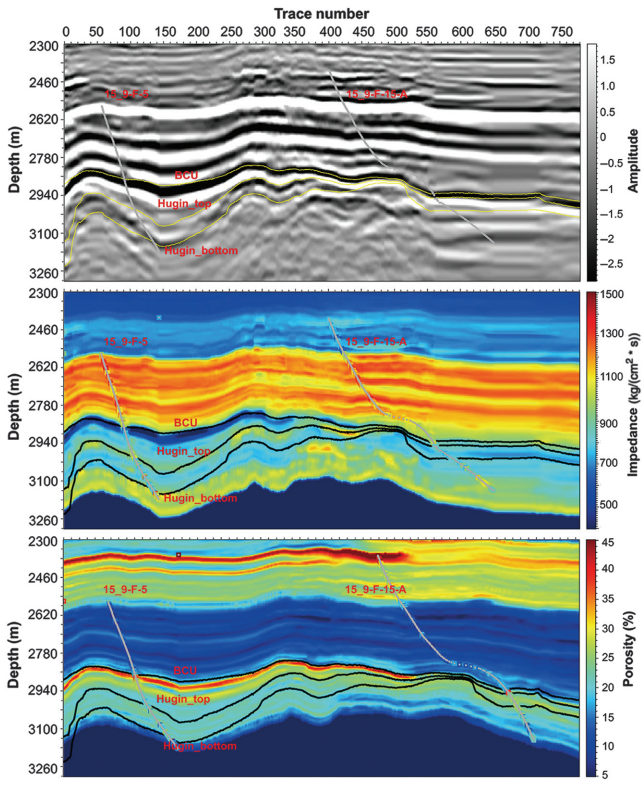

Figure 21. The profile of (a) seismic, (b) impedance, and (c) porosity connecting the wells of 15_9-F-5 and 15_9-F-15-A and containing horizons called BCU, Hugin_top, and Hugin_bottom.

DOI:10.1190/geo2021-0505.1

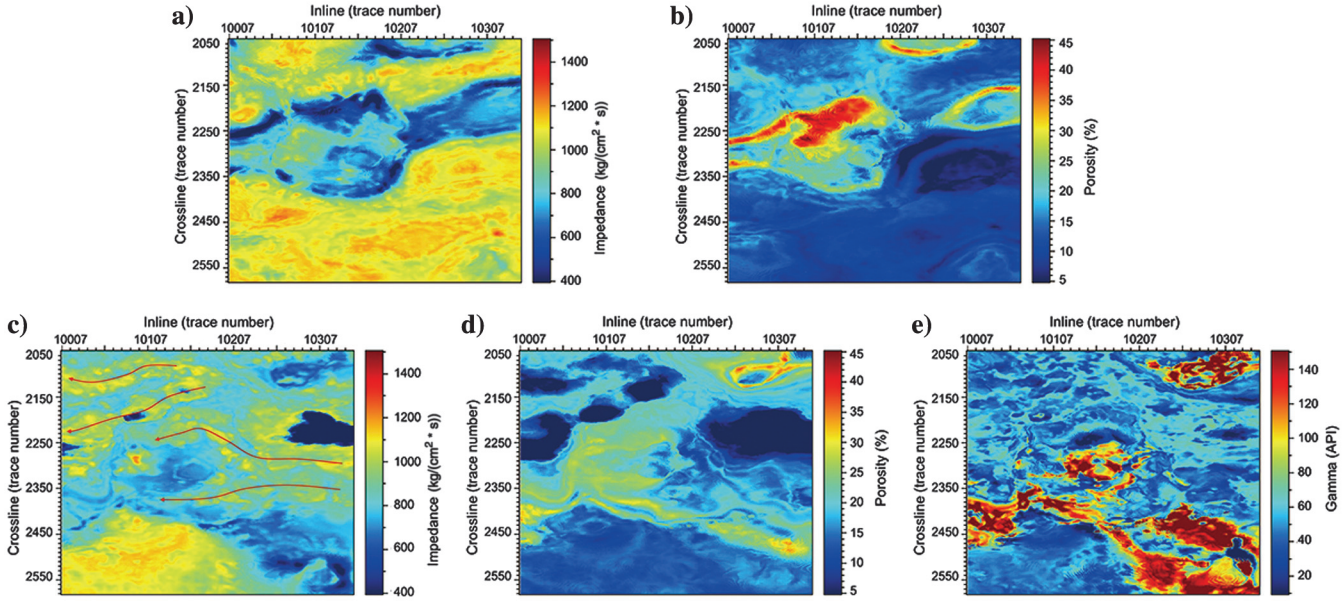

Figure 22. (a) Impedance slice of the top of BCU, (b) porosity slice of the top of BCU, (c) impedance slice of the top of the Hugin Formation, (d) porosity slice of the top of the Hugin Formation, and (e) gamma slice of the top of the Hugin Formation.

CONCLUSION

We propose a full workflow of seismic structural interpretation, horizon-guided well-log interpolation, and deep learning-based rock property estimation to build reasonable subsurface models. We have applied our workflow to the public Volve data set and obtain geologically reasonable results. In our workflow, we first implement some preprocessing and seismic-well ties to remove data anomalies and vertically align well logs with the seismic image. Second, we improve the provided horizons with automatic methods to fill the missing areas and follow consistent structures and extract more horizons. Then, an RGT volume is interpolated from these horizons, which represent seismic structural and stratigraphic features. Third, we obtain the initial models using RGT-based interpolation to be consistent with well-log properties and seismic structures. Finally, we predict the final models from seismic and well-log data using multiscale CNNs with the initial model as low-frequency constraints. The results show that our workflow can obtain reliable subsurface models with high vertical resolution.

From these tests, we suppose that the accuracy can be improved even with a simple network but more reasonable training and validation data sets. Our proposed workflow can be used with any data set that includes seismic amplitudes, well-log properties, and interpreted seismic structures, but the trained network in one survey cannot be directly used in another survey because of the variety of petrophysics in different areas. However, we can choose to retrain a network on a new survey because the 1D CNNs cost several minutes in our examples, which is completely acceptable. We also can attempt to use transfer learning to solve the generalization problem, which is based on the previously trained model and then adjusts parameters using new data. In addition, the proposed workflow also can be applied to further complicated modeling problems for which modeling results need strong constraints of sequence stratigraphy, such as facies modeling.

ACKNOWLEDGMENTS

This research was supported by the National Science Foundation of China under grant no. 42050104 and CNPC Innovation Foundation under grant no. 2020D-5007-0303.

DATA AND MATERIALS AVAILABILITY

Data associated with this research are available and can be obtained by contacting the corresponding author.

REFERENCES

Al-Anazi, A. F., and I. D. Gates, 2012, Support vector regression to predict porosity and permeability: Effect of sample size: Computers & Geosciences, **39**, 64–76, doi: 10.1016/j.cageo.2011.06.011.

Alfarraj, M., and G. AlRegib, 2018, Petrophysical property estimation from seismic data using recurrent neural networks: 88th Annual International Meeting, SEG, Expanded Abstracts, 2141–2146, doi: 10.1190/segam2018-2995752.1.

Alfarraj, M., and G. AlRegib, 2019, Semi-supervised learning for acoustic impedance inversion: 89th Annual International Meeting, SEG, Expanded Abstracts, 2298–2302, doi: 10.1190/segam2019-3215902.1.

Araya-Polo, M., J. Jennings, A. Adler, and T. Dahlke, 2018, Deep-learning tomography: The Leading Edge, **37**, 58–66, doi: 10.1190/tle37010058.1.

Biswas, R., M. K. Sen, V. Das, and T. Mukerji, 2019, Prestack and poststack inversion using a physics-guided convolutional neural network: Interpretation, **7**, no. 3, SE161–SE174, doi: 10.1190/INT-2018-0236.1.

Bosch, M., T. Mukerji, and E. F. Gonzalez, 2010, Seismic inversion for reservoir properties combining statistical rock physics and geostatistics: A review: Geophysics, **75**, no. 5, 75A165–75A176, doi: 10.1190/1.3478209.

Buland, A., and H. Omre, 2003, Bayesian linearized AVO inversion: Geophysics, **68**, 185–198, doi: 10.1190/1.1543206.

Caumon, G., P. Collon-Drouaillet, C. L. C. De Veslud, S. Viseur, and J. Sausse, 2009, Surface-based 3D modeling of geological structures: Mathematical Geosciences, **41**, 927–945, doi: 10.1007/s11004-009-9244-2.

Das, V., A. Pollack, U. Wollner, and T. Mukerji, 2019, Convolutional neural network for seismic impedance inversion: Geophysics, **84**, no. 6, R869–R880, doi: 10.1190/geo2018-0838.1.

Di, H., D. Gao, and G. AlRegib, 2019, Developing a seismic texture analysis neural network for machine-aided seismic pattern recognition and classification: Geophysical Journal International, **218**, 1262–1275, doi: 10.1093/gji/ggz226.

Dorn, G. A., 2013, Domain transform: A tool for imaging and interpreting geomorphology and stratigraphy in seismic volumes: The Leading Edge, **32**, 146–153, doi: 10.1190/tle32020146.1.

Dramsch, J. S., and M. Lüthje, 2018, Deep-learning seismic facies on state-of-the-art CNN architectures: 88th Annual International Meeting, SEG, Expanded Abstracts, 2036–2040, doi: 10.1190/segam2018-2996783.1.

Equinor, 2018, Volve Data Village dataset: Released under a license based on CC BY 4.0. [Online], https://data.equinor.com/, accessed 20 November 2020.

Fu, L.-Y., 2004, Joint inversion of seismic data for acoustic impedance: Geophysics, **69**, 994–1004, doi: 10.1190/1.1778242.

Geng, Z., X. Wu, Y. Shi, and S. Fomel, 2020, Deep learning for relative geologic time and seismic horizons: Geophysics, **85**, no. 4, WA87–WA100, doi: 10.1190/geo2019-0252.1.

Gholami, A., and M. D. Sacchi, 2012, A fast and automatic sparse deconvolution in the presence of outliers: IEEE Transactions on Geoscience and Remote Sensing, **50**, 4105–4116, doi: 10.1109/TGRS.2012.2189777.

González, E. F., T. Mukerji, and G. Mavko, 2008, Seismic inversion combining rock physics and multiple-point geostatistics: Geophysics, **73**, no. 1, R11–R21, doi: 10.1190/1.2803748.

Hale, D., 2010, Image-guided 3D interpolation of borehole data: 80th Annual International Meeting, SEG, Expanded Abstracts, 1266–1270, doi: 10.1190/1.3513074.

Hampson, D., T. Todorov, and B. Russell, 2000, Using multi-attribute transforms to predict log properties from seismic data: Exploration Geophysics, **31**, 481–487, doi: 10.1071/EG00481.

Hansen, T. M., K. Mosegaard, R. Pedersen-Tatalovic, A. Uldall, and N. L. Jacobsen, 2008, Attribute-guided well-log interpolation applied to low-frequency impedance estimation: Geophysics, **73**, no. 6, R83–R95, doi: 10.1190/1.2996302.

Jayr, S., E. Gringarten, A.-L. Tertois, J.-L. Mallet, and J.-C. Dulac, 2008, The need for a correct geological modelling support: The advent of the UVT-transform: First Break, **26**, 73–79, doi: 10.3997/1365-2397.26.10.28558.

Karimi, P., S. Fomel, and R. Zhang, 2017, Creating detailed subsurface models using predictive image-guided well-log interpolation: Interpretation, **5**, no. 3, T279–T285, doi: 10.1190/INT-2016-0051.1.

Kieft, R., C.-L. Jackson, G. Hampson, and E. Larsen, 2010, Sedimentology and sequence stratigraphy of the Hugin Formation, Quadrant 15, Norwegian sector, South Viking Graben: Geological Society of London, Geological Society, London, Petroleum Geology Conference Series, 157–176.

Labrunye, E., and C. Carn, 2015, Merging chronostratigraphic modeling and global horizon tracking: Interpretation, **3**, no. 2, SN59–SN67, doi: 10.1190/INT-2014-0130.1.

LeCun, Y., Y. Bengio, and G. Hinton, 2015, Deep learning: Nature, **521**, 436–444, doi: 10.1038/nature14539.

Lemon, A. M., and N. L. Jones, 2003, Building solid models from boreholes and user-defined cross-sections: Computers & Geosciences, **29**, 547–555, doi: 10.1016/S0098-3004(03)00051-7.

Lucas, A., M. Iliadis, R. Molina, and A. K. Katsaggelos, 2018, Using deep neural networks for inverse problems in imaging: Beyond analytical methods: IEEE Signal Processing Magazine, **35**, 20–36, doi: 10.1109/MSP.2017.2760358.

Ma, X.-Q., 2002, Simultaneous inversion of prestack seismic data for rock properties using simulated annealing: Geophysics, **67**, 1877–1885, doi: 10.1190/1.1527087.

Mallet, J.-L., 2002, Geomodeling: Oxford University Press.

Mallet, J.-L., 2014, Elements of mathematical sedimentary geology: The GeoChron model: EAGE Publications.

Mallick, S., 1995, Model-based inversion of amplitude-variations-with-offset data using a genetic algorithm: Geophysics, **60**, 939–954, doi: 10.1190/1.1443860.

Mosser, L., O. Dubrule, and M. J. Blunt, 2020, Stochastic seismic waveform inversion using generative adversarial networks as a geological prior: Mathematical Geosciences, **52**, 53–79, doi: 10.1007/s11004-019-09832-6.

Mustafa, A., M. Alfarraj, and G. AlRegib, 2019, Estimation of acoustic impedance from seismic data using temporal convolutional network: 89th Annual International Meeting, SEG, Expanded Abstracts, 2554–2558, doi: 10.1190/segam2019-3216840.1.

Naeini, E. Z., and D. Hale, 2015, Image- and horizon-guided interpolation: Geophysics, **80**, no. 3, V47–V56, doi: 10.1190/geo2014-0279.1.

Oldenburg, D., T. Scheuer, and S. Levy, 1983, Recovery of the acoustic impedance from reflection seismograms: Geophysics, **48**, 1318–1337, doi: 10.1190/1.1441413.

Puzyrev, V., A. Egorov, A. Pirogova, C. Elders, and C. Otto, 2019, Deep neural networks for 1D impedance inversion: Australasian Exploration Geoscience Conference, Extended Abstracts, doi: 10.1080/22020586.2019.12073187.

Richardson, A., 2018, Seismic full-waveform inversion using deep learning tools and techniques: arXiv preprint arXiv:1801.07232.

Sanghvi, Y., Y. Kalepu, and U. K. Khankhoje, 2020, Embedding deep learning in inverse scattering problems: IEEE Transactions on Computational Imaging, **6**, 46–56, doi: 10.1109/TCI.2019.2915580.

Sen, M. K., and P. L. Stoffa, 1991, Nonlinear one-dimensional seismic waveform inversion using simulated annealing: Geophysics, **56**, 1624–1638, doi: 10.1190/1.1442973.

Sen, S., and S. S. Ganguli, 2019, Estimation of pore pressure and fracture gradient in Volve field, Norwegian North Sea: Oil and Gas India Conference and Exhibition, SPE, Extended Abstracts.

Sheriff, R. E., and L. P. Geldart, 1995, Exploration seismology: Cambridge University Press.

Shi, Y., X. Wu, and S. Fomel, 2020, Waveform embedding: Automatic horizon picking with unsupervised deep learning: Geophysics, **85**, no. 4, WA67–WA76, doi: 10.1190/geo2019-0438.1.

Smith, G., and P. Gidlow, 1987, Weighted stacking for rock property estimation and detection of gas: Geophysical Prospecting, **35**, 993–1014, doi: 10.1111/j.1365-2478.1987.tb00856.x.

Souche, L., G. Iskenova, F. Lepage, and D. Desmarest, 2014, Construction of structurally and stratigraphically consistent structural models using the volume-based modelling technology: Applications to an Australian dataset: International Petroleum Technology Conference, Extended Abstracts, doi: 10.2523/IPTC-18216-MS.

Souche, L., F. Lepage, and G. Iskenova, 2013, Volume based modeling — Automated construction of complex structural models: 75th Annual International Conference and Exhibition Incorporating SPE EUROPEC 2013, EAGE, Extended Abstracts, cp-348, doi: 10.3997/2214-4609.20130037.

Stark, T. J., 2003, Unwrapping instantaneous phase to generate a relative geologic time volume: 73rd Annual International Meeting, SEG, Expanded Abstracts, 1707–1710, doi: 10.1190/1.1844072.

Stark, T. J., 2005a, Generation of a 3D seismic "Wheeler Diagram" from a high resolution age volume: 75th Annual International Meeting, SEG, Expanded Abstracts, 782–785, doi: 10.1190/1.2148275.

Stark, T. J., 2005b, System for multi-dimensional data analysis: U.S. Patent 6,850,845.

Stark, T. J., 2006, Visualization techniques for enhancing stratigraphic inferences from 3D seismic data volumes: First Break, **24**, 75–85, doi: 10.3997/1365-2397.24.1094.26926.

Sui, Y., and J. Ma, 2019, A nonstationary sparse spike deconvolution with anelastic attenuation: Geophysics, **84**, no. 2, R221–R234, doi: 10.1190/geo2017-0846.1.

Tarhan, C., and G. B. Akar, 2018, Convolutional neural networks analyzed via inverse problem theory and sparse representations: IET Signal Processing, **13**, 215–223, doi: 10.1049/iet-spr.2018.5220.

Varadi, M., P. Antonsen, M. Eien, and K. Häger, 1998, Jurassic genetic sequence stratigraphy of the Norwegian block 15/5 area, South Viking Graben, *in* B. A. Vining and S. C. Pickering, eds., Sequence stratigraphy — Concepts and applications: Norwegian Petroleum Society, Special Publications, 373–401.

Veeken, P., and M. Da Silva, 2004, Seismic inversion methods and some of their constraints: First Break, **22**, 47–70, doi: 10.3997/1365-2397.2004011.

Velis, D. R., 2008, Stochastic sparse-spike deconvolution: Geophysics, **73**, no. 1, R1–R9, doi: 10.1190/1.2790584.

Wang, K., L. Bandura, D. Bevc, S. Cheng, J. DiSiena, A. Halpert, K. Osypov, B. Power, and E. Xu, 2019, End-to-end deep neural network for seismic inversion: 89th Annual International Meeting, SEG, Expanded Abstracts, doi: 10.1190/segam2019-3216464.1.

Wang, L., Q. Zhao, J. Gao, Z. Xu, M. Fehler, and X. Jiang, 2016, Seismic sparse-spike deconvolution via Toeplitz-sparse matrix factorization: Geophysics, **81**, no. 3, V169–V182, doi: 10.1190/geo2015-0151.1.

Wu, X., 2017a, Building 3D subsurface models conforming to seismic structural and stratigraphic features: Geophysics, **82**, no. 3, IM21–IM30, doi: 10.1190/geo2016-0255.1.

Wu, X., 2017b, Structure-, stratigraphy-, and fault-guided regularization in geophysical inversion: Geophysical Journal International, **210**, 184–195, doi: 10.1093/gji/ggx150.

Wu, X., L. Liang, Y. Shi, and S. Fomel, 2019a, FaultSeg3D: Using synthetic data sets to train an end-to-end convolutional neural network for 3D seismic fault segmentation: Geophysics, **84**, no. 3, IM35–IM45, doi: 10.1190/geo2018-0646.1.

Wu, X., Y. Shi, S. Fomel, L. Liang, Q. Zhang, and A. Z. Yusifov, 2019b, FaultNet3D: Predicting fault probabilities, strikes, and dips with a single convolutional neural network: IEEE Transactions on Geoscience and Remote Sensing, **57**, 9138–9155, doi: 10.1109/TGRS.2019.2925003.

Wu, X., and G. Zhong, 2012, Generating a relative geologic time volume by 3D graph-cut phase unwrapping method with horizon and unconformity constraints: Geophysics, **77**, no. 4, O21–O34, doi: 10.1190/geo2011-0351.1.

Wu, Y., and G. A. McMechan, 2018, Feature-capturing full waveform inversion using a convolutional neural network: 88th Annual International Meeting, SEG, Expanded Abstracts, 2061–2065, doi: 10.1190/segam2018-2963265.1.

Yan, S., and X. Wu, 2021, Seismic horizon extraction with dynamic programming: Geophysics, **86**, no. 2, IM51–IM62, doi: 10.1190/geo2020-0039.1.
Yuan, S., S. Wang, C. Luo, and Y. He, 2015, Simultaneous multitrace impedance inversion with transform-domain sparsity promotion: Geophysics, **80**, no. 2, R71–R80, doi: 10.1190/geo2014-0065.1.
Zhang, G., Z. Wang, and Y. Chen, 2018, Deep learning for seismic lithology prediction: Geophysical Journal International, **215**, 1368–1387, doi: 10.1093/gji/ggy344.
Zhang, R., and J. Castagna, 2011, Seismic sparse-layer reflectivity inversion using basis pursuit decomposition: Geophysics, **76**, no. 6, R147–R158, doi: 10.1190/geo2011-0103.1.
Zheng, Y., Q. Zhang, A. Yusifov, and Y. Shi, 2019, Applications of supervised deep learning for seismic interpretation and inversion: The Leading Edge, **38**, 526–533, doi: 10.1190/tle38070526.1.
Zhu, L., C. Zhang, M. Li, X. Pan, and J. Sun, 2012, Building 3D solid models of sedimentary stratigraphic systems from borehole data: An automatic method and case studies: Engineering Geology, **127**, 1–13, doi: 10.1016/j.enggeo.2011.12.001.

Biographies and photographs of the authors are not available.